

# Dependence of the electronic structure of self-assembled InGaAs/GaAs quantum dots on height and composition

Gustavo A. Narvaez, Gabriel Bester, and Alex Zunger  
*National Renewable Energy Laboratory, Golden, Colorado 80401*  
 (Dated: August 29, 2018)

While electronic and spectroscopic properties of self-assembled  $\text{In}_{1-x}\text{Ga}_x\text{As}/\text{GaAs}$  dots depend on their shape, height and alloy compositions, these characteristics are often not known accurately from experiment. This creates a difficulty in comparing measured electronic and spectroscopic properties with calculated ones. Since simplified theoretical models (effective mass,  $k\cdot p$ , parabolic models) do not fully convey the effects of shape, size and composition on the electronic and spectroscopic properties, we offer to bridge the gap by providing accurately calculated results as a function of the dot height and composition. Prominent features of our results are the following. (i) Regardless of height and composition, the confined electron energy levels form shells of nearly degenerate states with a predominant orbital “s”, “p”,  $\dots$  character. In contrast, the confined hole energy levels form shells only in flat dots and near the highest hole level (HOMO). (ii) In alloy dots, the *electrons’* “s-p” splitting depends weakly on height, while the “p-p” splitting depends non-monotonically—due to alloy fluctuations. In pure, non-alloyed InAs/GaAs dots, *both* these splittings depend weakly on height. Further, the “s-p” splitting is larger while the “p-p” has nearly the same magnitude. For *holes* levels in alloy dots, the “s-p” splitting decreases with increasing height (the splitting in tall dots being about 4 times smaller than in flat dots), whereas the “p-p” splitting remains nearly unchanged. Shallow, pure non-alloyed dots have a “s-p” splitting of nearly the same magnitude, whereas the “p-p” splitting is about three times larger. (iii) As height increases, the “s” and “p” character of the wavefunction of the HOMO becomes mixed, and so does the heavy- and light-hole character. (iv) In alloy dots, regardless of height, the wavefunction of low-lying hole states are localized inside the dot. Remarkably, in non-alloyed InAs/GaAs dots these states become localized at the interface as height increases. The localized states are nearly degenerate and polarized along  $[1\bar{1}0]$  and  $[110]$ . This localization is driven by the peculiarities of the biaxial strain present in the nanostructure.

## I. INTRODUCTION

The electronic structure and spectroscopic properties of quantum dots, including excitons,<sup>1,2,3,4,5,6</sup> charged excitons,<sup>2,3</sup> multiexcitons,<sup>3,4,5</sup> and excitonic fine-structure,<sup>6</sup> all depend on the size and shape of the dots. This dependence reflects both quantum confinement effects, as well as shape-induced band-folding and inter-band coupling.<sup>7</sup> *Simulations* of electronic structure and spectroscopic properties of quantum dots<sup>8,9,10,11,12,13,14</sup> must naturally assume the size and shape of the dot. On the other hand, *measurements* of spectroscopic properties of a dot<sup>1,2,3,4,5,6</sup> are rarely accompanied by accurate measurements of the size and shape of the GaAs-covered dot, except in rare cases where detailed cross-sectional scanning tunneling microscopy experiments are performed, such as in Refs. 15,16,17. This situation creates a significant difficulty, if not a crisis, in interpreting spectroscopic data on quantum dots, and in critically testing various theoretical approaches. Thus, in reality one is often forced to address the inverse problem,<sup>13</sup> namely, fit the spectroscopic data to a theoretical model by using the size and shape as adjustable parameters. The difficulty with this approach is threefold: First, in this approach all theories, no matter how naïve, ultimately work by virtue of forcing a fit to experiment, even if the assumptions entering the theory may seem unjustified in their own right (e.g. assuming single-band effective mass; neglect of strain; neglect of spin-orbit coupling.) Second, there are

usually too many free-parameters, which involve not only non-trivial shapes, but also unknown composition profiles (e. g.,  $\text{In}_{1-x}\text{Ga}_x\text{As}$  dots). Third, since the relationship between shape and spectroscopic properties is model dependent, unrealistic shapes are often deduced. For example, in simple effective-mass,<sup>12,18,19</sup>  $k\cdot p$ ,<sup>20</sup> or parabolic models the “p” and “d” levels of electrons and holes are degenerate if one assumes spherical, lens-shaped, cubic, or cylindrical dots. In contrast, in more advanced *atomistic* models—like empirical pseudopotential<sup>21,22,23</sup> or tight binding<sup>24</sup>—those levels are split even for the above mentioned ideal shapes, resulting in clear spectroscopic signatures. To fit measured spectroscopic signatures of actual dots by simple theoretical models, one needs to assume at the outset irregular shapes. For instance, Dekel *et al.*<sup>5</sup> needed to assume a parallelepipedal box to explain their multiexciton data on non-alloyed InAs/GaAs dots; and Ferreira assumed shape distortions to explain fine structure.<sup>25</sup> Such assumptions are not needed in atomistic approaches to modeling.

In this work we have used a high-level atomistic approach to predict the spectroscopic characteristics of  $\text{In}_{1-x}\text{Ga}_x\text{As}/\text{GaAs}$  self-assembled dots as a function of the most crucial geometric parameter, namely the height. We calculate strain profiles, “p-” and “d-” level splittings as well as electron and hole wavefunctions. While ultimately it will be necessary for experimentalists to report the size, shape, and composition profile to which their spectroscopic data correspond, the type of study reported here may be used to bridge, in the interim, spectroscopy

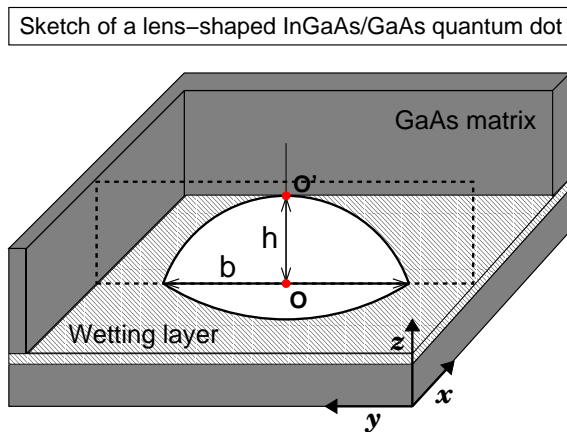


FIG. 1: Sketch of the geometry of self-assembled  $\text{In}_{1-x}\text{Ga}_x\text{As}/\text{GaAs}$  quantum dots. A section of the GaAs matrix (grey) has been omitted for clarity. The dot (white) is lens shaped with base diameter  $b$  and height  $h$ . The dot lies on top of a 1-monolayer-thick  $\text{In}_{1-x}\text{Ga}_x\text{As}$  wetting layer. Two auxiliary features are shown: (i) A plane that bisects the dot (dashed lines) and (ii) the line  $\overleftrightarrow{OO'}$ , which pierces the dot through the center along the  $[001]$  direction.

with theory without clouding the issue by severe theoretical approximations. Similar studies were carried out by the group of Bimberg in Refs. 26,27,28,29, by Shumway *et al.* in Ref. 13, by Williamson *et al.* in Ref. 14, by Kim *et al.* in Ref. 30 and by Pryor in Ref. 31.

## II. METHODS AND THEIR ILLUSTRATION

### A. Choice of dot geometries

Among several geometries, Stranski-Krastanow quantum dots growth in lens shape.<sup>32</sup> Hence, we focus on lens-shaped, self-assembled  $\text{In}_{1-x}\text{Ga}_x\text{As}/\text{GaAs}$  quantum dots (QDs). In addition, we include a 1-monolayer-thick  $\text{In}_{1-x}\text{Ga}_x\text{As}$  wetting layer (WL). Figure 1 shows a sketch of the geometry of the nanostructure. (QD+WL+GaAs matrix). We focus on dots with  $x = 0.4$  and pure InAs. The QDs have circular base with diameter  $b = 252 \text{ \AA}$  and height  $h$  in the interval  $20 \text{ \AA} - 75 \text{ \AA}$ .

### B. Strain relaxation done via atomistic, not continuum elasticity

The position-dependent strain profiles present in the nanostructure are usually addressed within (harmonic) *continuum* elasticity (CE) theory.<sup>33,34</sup> Notwithstanding, strain profiles can also be calculated within atomistic elasticity (AE) in the form of a valence force field.<sup>35</sup> In AE the strain energy is expressed in terms of atomic positions and interatomic force constants. While the force constants are fit to the elastic constants  $C_{11}$ ,  $C_{12}$  and

$C_{44}$ , much like in CE, expressing the strain in terms of atomic positions contains much more information than expressing strain in terms of CE coordinates. For example, a square-based pyramid has a  $C_{4v}$  point group symmetry if described by CE. This means that the  $[110]$  and  $[\bar{1}10]$  facets are taken to be equivalent. In this case, all “p” energy levels are degenerate. However, in AE the point group symmetry of a square-based pyramid made of InAs is  $C_{2v}$ . In this case, the  $[110]$  and  $[\bar{1}10]$  facets are symmetry-inequivalent and “p” levels are split.

In general, three interrelated sources are responsible for the splitting of the “p” states.<sup>36</sup> A quantum dot with a base that globally possesses inversion symmetry in the  $(001)$  plane—like a lens, a truncated pyramid or a truncated cone—has in reality the lower  $C_{2v}$  symmetry (for pure, non-alloyed InAs/GaAs dots), which originates from the underlying zinc-blende atomic lattice. Thus, the *first source* is the lack of inversion symmetry in the  $C_{2v}$  point group, which manifests itself around the dot-matrix interfaces where the  $[110]$  and  $[\bar{1}10]$  directions are inequivalent. The *second source* is the propagation of the strain field towards the center of the dot as a consequence of the atomic relaxation. The *third source* is the piezoelectric effect (which magnitude is presently under debate<sup>36</sup>) that arises from the strain field of  $C_{2v}$  symmetry. It should be noted that approximations used in previous calculations of the piezoelectric effect<sup>37,38</sup> have been shown to be crude and further investigations have been called for.<sup>36</sup>

Our choice of AE is based on a generalization of Keating model to 3 terms—bond-bending, bond stretching and their cross terms.<sup>14</sup> We fit the elastic constants  $C_{11}$ ,  $C_{12}$  and  $C_{44}$  of zinc-blende InAs and GaAs, as well as the correct dependence of the Young’s modulus with pressure for both materials. In the  $\text{In}_{1-x}\text{Ga}_x\text{As}$  alloy system, the bond-stretching and the bond-stretching/bond-bending cross-term parameters for the mixed cation Ga-As-In bond angle are taken as the algebraic average of the In-As-In and Ga-As-Ga values. While the ideal bond angle is  $109^\circ$  for the pure zinc-blende crystal, to satisfy Vegard’s law for the alloy volume, the value of  $110.5^\circ$  was used for the mixed bond angle. AE is superior to CE in that it does not assume harmonicity—in fact, anharmonic effects can be explicitly included<sup>39</sup> into the valence force field.<sup>35</sup>

Here, we calculate the position-dependent strain tensor  $\tilde{\varepsilon}(\mathbf{R})$  within the atomistic elasticity approach. To calculate the strain tensor cubic components  $\varepsilon_{ij}$  ( $i, j = x, y, z$ ), we proceed in two steps: (1) We relax the atomic positions within the supercell in order to minimize the elastic energy, which is given by a generalized valence force field.<sup>14</sup> (2) We relate the relaxed (equilibrium) atomic positions with the unrelaxed atomic positions via strain tensor.<sup>34</sup> At each equilibrium position  $\mathbf{R}_l$  of atom  $l$  we identify the tetrahedron formed by its 4 nearest neighbors. This tetrahedron is distorted in comparison to the unrelaxed tetrahedron. Thus, the three edges of these tetrahedra that are determined by the vectors connect-

ing the four neighbors can be related by the strain tensor  $\tilde{\varepsilon}$  as follows.

$$\begin{pmatrix} \mathbf{R}_{al,x} & \mathbf{R}_{bl,x} & \mathbf{R}_{cl,x} \\ \mathbf{R}_{al,y} & \mathbf{R}_{bl,y} & \mathbf{R}_{cl,y} \\ \mathbf{R}_{al,z} & \mathbf{R}_{bl,z} & \mathbf{R}_{cl,z} \end{pmatrix} = \begin{pmatrix} 1 + \varepsilon_{xx} & \varepsilon_{yx} & \varepsilon_{zx} \\ \varepsilon_{xy} & 1 + \varepsilon_{yy} & \varepsilon_{yz} \\ \varepsilon_{xz} & \varepsilon_{yz} & 1 + \varepsilon_{zz} \end{pmatrix} \times \begin{pmatrix} \mathbf{R}_{al,x}^0 & \mathbf{R}_{bl,x}^0 & \mathbf{R}_{cl,x}^0 \\ \mathbf{R}_{al,y}^0 & \mathbf{R}_{bl,y}^0 & \mathbf{R}_{cl,y}^0 \\ \mathbf{R}_{al,z}^0 & \mathbf{R}_{bl,z}^0 & \mathbf{R}_{cl,z}^0 \end{pmatrix}, \quad (1)$$

where  $\mathbf{R}_{al}$ ,  $\mathbf{R}_{bl}$ , and  $\mathbf{R}_{cl}$  are the 3 vectors that connect, respectively, neighbors 1 and 2, 2 and 3, and 3 and 4 in the equilibrium, distorted tetrahedron that encloses atom  $l$ .  $\mathbf{R}_{al}^0$ ,  $\mathbf{R}_{bl}^0$ , and  $\mathbf{R}_{cl}^0$  are the corresponding vectors (edges) in the unrelaxed tetrahedron. From Eq. (1), the cubic strain tensor components are calculated by a matrix inversion.

Figure 2 shows the biaxial strain

$$B = \sqrt{(\varepsilon_{xx} - \varepsilon_{yy})^2 + (\varepsilon_{yy} - \varepsilon_{zz})^2 + (\varepsilon_{zz} - \varepsilon_{xx})^2} \quad (2)$$

and the hydrostatic distortion (isotropic strain)  $I = \text{Tr}(\tilde{\varepsilon})$  as a function of dot height. The results presented correspond to the strain values on a planar section in the [100] direction that bisects the dot (see Fig. 1). The spikes in the dot and wetting layer region are a consequence of the random arrangement of In and Ga atoms. Thus, the spikes structure significantly changes from dot to dot. Two additional features are also prominent. (i) The biaxial strain at the dot-matrix interface, located near the top of the dot, increases with height and slowly decays off. This decay is faster as the dot becomes taller. The latter can be understood by considering the dot as a spherical cap inscribed in a sphere of radius  $\rho_0 = [h^2 + (b/2)^2]/2h$  (the *taller* the dot, the *smaller*  $\rho_0$ ) and by assuming that the decay of  $B$  outside the dot is qualitatively well described by  $(\rho_0/\rho)^3$ , which is the radial dependence of the biaxial strain outside a continuum, elastic sphere of radius  $\rho_0$  embedded in a lattice-mismatched medium.<sup>40</sup> Here,  $\rho$  is the radial distance from the sphere surface. In our simulations,  $\text{Tr}(\tilde{\varepsilon})$  shows a similar trend as  $B$ . (ii) Due to the underlying zincblende atomic structure, the biaxial strain drops to zero along the [011] and [01 $\bar{1}$ ] directions, as well as along their equivalent crystallographic directions. (See white arrows in Fig. 2.) This feature is robust upon changes in height, being present for all the quantum dots we considered.

### C. The single-particle electronic structure is calculated via pseudopotential plane-wave method instead of $\mathbf{k} \cdot \mathbf{p}$

To calculate the energies and wavefunctions of electron and hole states in the quantum dot, we use the empirical pseudopotential method of Wang and Zunger.<sup>21</sup> This

approach combines a pseudopotential description of the single-particle Hamiltonian with the linear combination of bulk bands (LCBB) method to solve for the energies and wavefunctions.<sup>21</sup> In this method, the Hamiltonian reads

$$\mathcal{H} = -\frac{\beta}{2}\nabla^2 + V^{SO} + \sum_{\alpha=\text{In,Ga,As}} \sum_l v_{\alpha}(\mathbf{R} - \mathbf{R}_l^{\alpha}; \tilde{\varepsilon}), \quad (3)$$

where  $\beta$  is an empirical parameter that accounts for non-locality effects;  $V^{SO}$  is a non-local empirical operator that describes the spin-orbit interaction;<sup>14</sup>  $v_{\alpha}(\eta; \tilde{\varepsilon})$  is a screened pseudopotential (for atom of type  $\alpha$ ) that depends on strain; and  $\mathbf{R}_l^{\alpha}$  is the relaxed vector position of atom  $l$  of type  $\alpha$ . The dependence of the atomic pseudopotential on strain transfers to the electronic Hamiltonian the information on atomic displacements. The strain-dependent pseudopotential reads

$$v_{\alpha}(\mathbf{R} - \mathbf{R}_l^{\alpha}; 0)[1 + \gamma_{\alpha} \text{Tr}(\tilde{\varepsilon})], \quad (4)$$

where  $\gamma_{\alpha}$  is a fitting parameter. It should be noted that  $v_{\alpha}(\mathbf{R} - \mathbf{R}_l^{\alpha}; \tilde{\varepsilon})$  is fit to *bulk* properties of GaAs and InAs, including bulk band structures, experimental deformation potentials and effective masses, and LDA-determined band offsets. In order to improve the transferability of pseudopotential  $v_{\alpha}(\mathbf{R} - \mathbf{R}_l^{\alpha}; \tilde{\varepsilon})$ , a simple dependence on the chemical environment of atom  $\alpha$  is introduced. For instance, for  $\alpha = \text{As}$  in an environment of  $p$  Ga atoms and  $p - 4$  In atoms we use

$$v_{As}^{(p)} = \frac{(4-p)}{p} v_{As}(\text{InAs}) + \frac{p}{4} v_{As}(\text{GaAs}). \quad (5)$$

The pseudopotentials used in this work have been successfully tested for quantum wells.<sup>14</sup>

The wavefunction of state  $i$  is  $\psi_i(\mathbf{R})$ , which satisfies  $\mathcal{H}\psi_i = \mathcal{E}_i\psi_i$ , is expanded in bulk Bloch states  $u_{n,\mathbf{k}}^{(M)}(\mathbf{R})$  of material  $M$ . [It should be noted that the bulk materials ( $M$ ) can be strained.<sup>21</sup>] Namely,

$$\psi_i(\mathbf{R}) = \sum_M \sum_{n,\mathbf{k}} C_{M;n,\mathbf{k}}^{(i)} \left[ \frac{1}{\sqrt{N}} u_{n,\mathbf{k}}^{(M)}(\mathbf{R}) e^{i\mathbf{k}\cdot\mathbf{R}} \right], \quad (6)$$

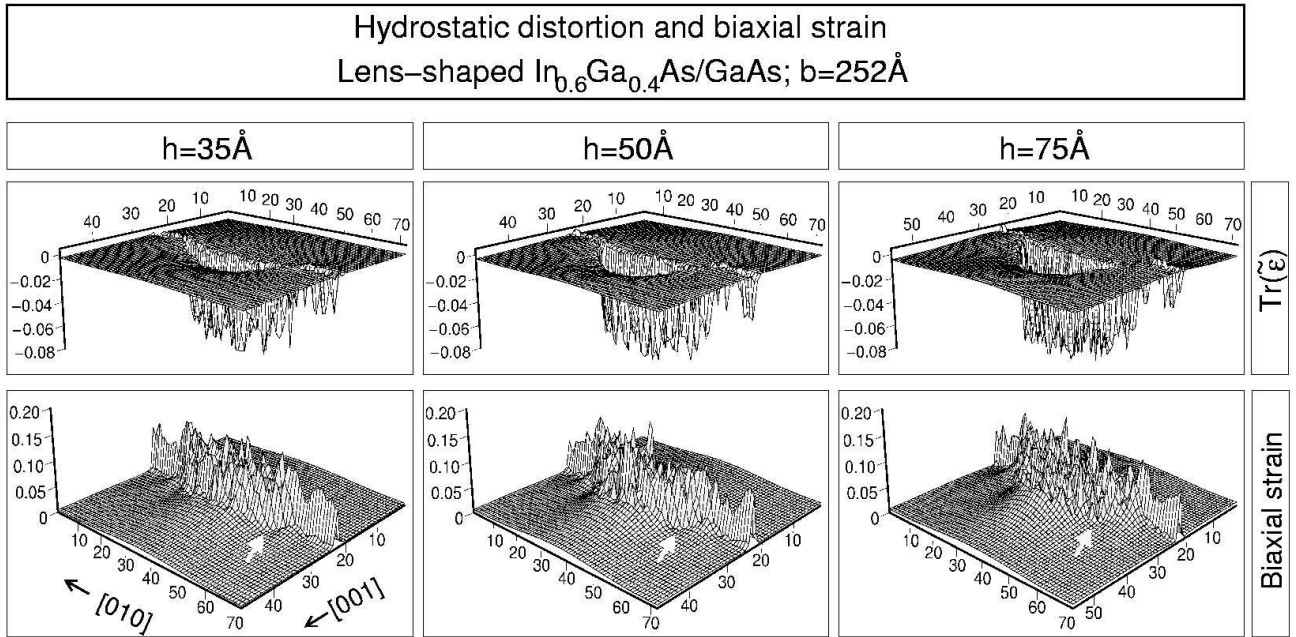


FIG. 2: Hydrostatic distortion [ $\text{Tr}(\tilde{\epsilon})$ ; top] and biaxial strain (bottom) as a function of dot's height plotted on a planar section that is normal to  $[100]$  and bisects the dot (see Fig. 1). Positions are measured in units of  $a_{\text{GaAs}} = 5.65 \text{\AA}$ . The wetting layer (WL) strain appears prominently. Alloy fluctuations make the strain profiles sample dependent. Two robust features emerge: (i) The biaxial strain at the top of the dot increases with height and slowly decays off. The taller the dot the faster this decay.  $\text{Tr}(\tilde{\epsilon})$  shows a similar trend. (ii) The underlying zincblende atomic structure causes the strain to rapidly drop to zero along the  $[01\bar{1}]$  and  $[0\bar{1}1]$  directions. Arrows indicate this feature.

where,  $n$  and  $\mathbf{k}$  indicate the band-index and wave-vector of the Bloch state, respectively; and  $N$  is the number of primary cells contained in a supercell that encloses the quantum dot. Thus, by diagonalizing the Hamiltonian [Eq. (3)] in the Bloch states basis we find the coefficients  $C_{M;n,\mathbf{k}}^{(i)}$ . The calculated wavefunctions  $\psi_i(\mathbf{R})$  are 2-fold, Kramers degenerate, so we have omitted the spin index  $\sigma$ . This representation for the wave function is very different from the familiar k-p method in that in the latter approach the basis set is constructed only from states near the Brillouin zone center ( $\Gamma$ ), while here we use a full-zone description. Further, in k-p one is restricted to just one or two Bloch bands at  $\Gamma$  ( $8 \times 8$  representing two Bloch bands) while here we consider  $n$  Bloch bands. In Appendix A, we present an assessment of the convergence of energy levels  $\mathcal{E}_i$  as a function of the expansion parameters in Eq. (6).

#### D. Strain-modified band offsets

While we describe the effects of strain on the electronic structure atomistically as shown in Eq. 3, here, for *illustrative purposes only*, we calculate the conduction (electron) and valence (hole) strain-modified band offsets (confining potentials) present in the quantum dot by coupling strain to k-p-like equations. At each 8-atom unit cell in the supercell we diagonalize the conduction and valence (including spin-orbit coupling) band strain

Hamiltonians that Wei and Zunger put forward in Ref. 41. Figure 3 shows the calculated strain-modified band offsets for electrons and holes along the line  $\overleftrightarrow{OO'}$  indicated in Fig. 1. Electron band offset appears in the upper panel, whereas thick and thin lines in the lower panel show the first and second holes offsets, respectively. We note the following features. (i) The band offsets (Fig. 3) inherit the jagged nature of the strain fields (Fig. 2). Inside the quantum dot (region “D” in Fig. 3), alloy fluctuations lead to a small mixing in the heavy-hole (HH) and light-hole (LH) character of the band offsets. (ii) Regardless of the dot height, the higher energy hole band offset has HH character inside the dot and LH outside. Conversely, the lower energy hole band offset has LH character inside and HH outside. (iii) The increase of biaxial strain at the dot-matrix interface that occurs as the height increases (Fig. 2) is reflected in the increase (decrease) of the higher (lower) energy hole band offset. (See arrows in Fig. 3). In particular, for tall dots, the decrease of the lower energy hole offset at the interface leads to the formation of a *pocket* in the band offset.

#### E. Orbital and Bloch character of wavefunctions

The single-band effective mass model predicts that in the continuum limit, in which lens-shaped dots have full axial symmetry, the confined energy levels will form shells

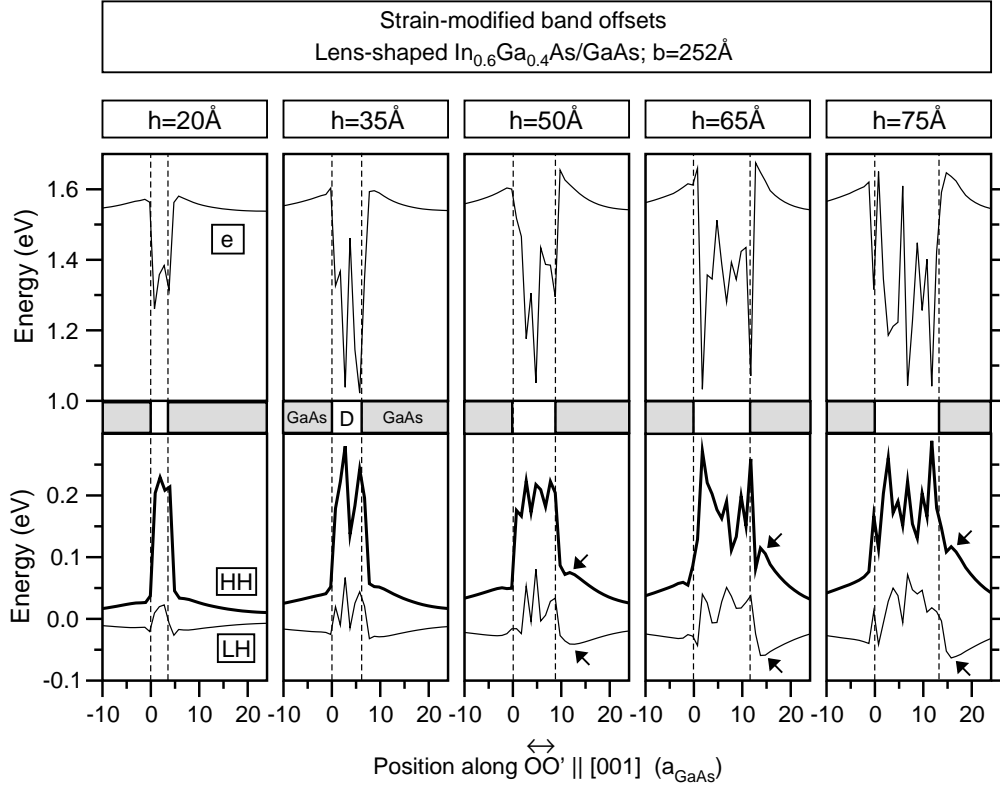


FIG. 3: Strain-modified band offsets for electrons (upper panel,  $e$ ), and first and second holes (lower panel; thick and thin lines, respectively) along the  $\overleftrightarrow{OO'} \parallel [001]$  as a function of height. (See Fig. 1.) In the dot region (indicated with a  $D$ ) the offsets are irregular (jagged) due to alloy fluctuations. These irregularities are more noticeable as the height increases. Outside  $D$  the heavy-hole (HH) and light-hole (LH) character reverses. Arrows indicate “pocket” formation in the second hole band offset as the dot’s height increases.

of degenerate states with *definite* angular momentum  $l = 0, 1, 2, \dots$ .<sup>44</sup> Thus, the *orbital* character of the confined levels will be *pure* “s”, “p”, “d”, etc. However, when the correct symmetry of the dot is taken in to account, as it is the case when using our atomistic pseudopotential method, the confined energy levels can have mixed orbital character. To quantify the degree of mixing, we analyse the single-particle wavefunctions  $\psi_i(\mathbf{R})$  by projecting their *envelopes* on eigenfunctions of the axial ( $\parallel z$ , see Fig. 1) angular momentum  $e^{im\phi}/\sqrt{2\pi}$  and determine the orbital (angular) character. The latter given by

$$A_{m,n}^{(i)} = \int dz \int d\rho \rho \left| \int d\phi f_n^{(i)}(\rho, \phi, z) \frac{e^{im\phi}}{\sqrt{2\pi}} \right|^2. \quad (7)$$

In Eq. (7), we have used cylindrical coordinates, i. e.  $\mathbf{R} = (\rho, \phi, z)$ , and written the  $\Gamma$ -derived envelope function as

$$f_n^{(i)}(\rho, \phi, z) = \sum_M \sum_{\mathbf{k}} \sum_{n'} C_{M;n,\mathbf{k}}^{(i)} \langle u_{n,\mathbf{k}}^{(M)} | u_{n',\Gamma}^{(M)} \rangle \frac{e^{i\mathbf{k}\cdot\mathbf{R}}}{\sqrt{N}}. \quad (8)$$

The Bloch character of the hole wavefunctions  $\psi_i^h(\mathbf{R})$  in the quantum dot depends on strain as well as band coupling. To study the extent to which the Bloch character is HH, LH, and SO, we proceed similarly and project the envelope of  $\psi_i^h(\mathbf{R})$  on the total-angular-momentum basis  $|J, J_z\rangle$  ( $\{|3/2, \pm 3/2\rangle, |3/2, \pm 1/2\rangle, |1/2, \pm 1/2\rangle\}$ ).

#### F. Exciton energy levels are obtained via the screened configuration interaction approach, not perturbation theory

We calculate the exciton energy levels  $E_\nu$  by using the configuration interaction method as proposed in Ref. 42. Briefly, in this method, the exciton states

$$\Psi_\nu = \sum_{i,j} C_{ij}^{(\nu)} |e_i h_j\rangle, \quad (9)$$

where  $\{|e_i h_j\rangle\}$  denotes a basis of single-substitution Slater determinants (configurations), in which an electron is promoted from  $\psi_j^{(h)}(\mathbf{R})$  to  $\psi_i^{(e)}(\mathbf{R})$ . The CI method would deliver the exact exciton ground and excited states in the case of a complete basis. However, we

*truncate* this basis and consider all the possible configurations build out of  $n_e$  electron and  $n_h$  hole confined states. The coefficients  $C_{ij}^{(\nu)}$  arise from the diagonalization of the exciton Hamiltonian. The direct ( $J_{ij} = \Gamma_{j,i}^{i,j}$ )

and exchange ( $K_{ij} = \Gamma_{i,j}^{i,j}$ ) electron-hole Coulomb integrals that enter the calculation are derived from the Coulomb scattering matrix elements

$$\Gamma_{k,l}^{i,j} = e^2 \int \int d\mathbf{R}d\mathbf{R}' \frac{[\psi_i^{(h)}(\mathbf{R})]^* [\psi_j^{(e)}(\mathbf{R}')]^* \psi_k^{(e)}(\mathbf{R}') \psi_l^{(h)}(\mathbf{R})}{\epsilon(\mathbf{R}, \mathbf{R}') |\mathbf{R} - \mathbf{R}'|} \quad (10)$$

The microscopic, phenomenological dielectric constant  $\epsilon(\mathbf{R}, \mathbf{R}')$  that screens the interaction is calculated within the Thomas-Fermi model proposed by Resta.<sup>43</sup> We do not use simple perturbation theory where the exciton is described via a Coulomb-corrected single-particle band gap  $(\mathcal{E}_i^e - \mathcal{E}_j^h) - J_{ij}$ ; here,  $\mathcal{E}_i^e$  and  $\mathcal{E}_j^h$  are the energies of electron level  $i$  and hole level  $j$ , respectively.

### III. RESULTS

We now present the effects of height and composition on the energies of confined levels and their splittings, wavefunctions of selected confined electron and hole levels, and the lowest transition energy of the exciton.

#### A. Energies of confined levels: “p” levels split even for ideal lens-shape dots

The confined electron and hole energy levels are respectively labeled as  $\mathcal{E}_i^e$  and  $\mathcal{E}_i^h$ , where  $i = 0, 1, \dots$  is an orbital quantum number. The corresponding wavefunctions are  $\psi_n^{(e)}(\mathbf{r})$  and  $\psi_n^{(h)}(\mathbf{r})$ . Each of the confined states are 2-fold, Kramers degenerate. We label the  $i = 0$  electron and hole states as LUMO and HOMO, respectively. The first 20 electron and hole energy levels of an  $\text{In}_{0.6}\text{Ga}_{0.4}\text{As}/\text{GaAs}$  dot appear in Figure 4. The electron and hole energies are measured, respectively, from the bottom of the conduction band (CBM)  $E_c(\text{GaAs}) = -4.093 \text{ eV}$  (calculated bulk electron affinity) and from the top of the valence band (VBM)  $E_v(\text{GaAs}) = -5.620 \text{ eV}$  (calculated bulk ionization potential) of bulk GaAs. For all heights, the confined electron states form groups (*shells*) of *non-degenerate* levels.<sup>44</sup> In turn, this shell structure can only be identified for the first few hole levels (near HOMO) in shallow dots (up to  $h = 50 \text{ \AA}$ ). For taller dots, the holes show no shell structure. The number of confined electron states is significantly smaller than that of holes. While for the tallest dot there are 10 confined electron states, more than 150 hole states are confined in all the considered dots. When comparing the results for  $h = 35 \text{ \AA}$  with the first 20 electron and hole energy levels (not shown) in a

lens-shaped, non-alloyed  $\text{InAs}/\text{GaAs}$  dot, we find that (i) the electron levels form shells that have a bigger average separation (55 meV vs 45 meV in  $\text{In}_{0.6}\text{Ga}_{0.4}\text{As}/\text{GaAs}$ ), (ii) the hole energy level structure near the HOMO is significantly different (see splittings in Fig. 5) and (iii) the single-particle gap  $\mathcal{E}_0^e - \mathcal{E}_0^h$  is smaller (see Fig. 10).

*Energy splittings.*—The “s-p” energy splitting  $\mathcal{E}_1 - \mathcal{E}_0$  and “p-p” splitting  $\mathcal{E}_2 - \mathcal{E}_1$  for electrons and holes are shown in Figure 7 as a function of the dot height. (The dots’ single-particle gap is also indicated.) Two features emerge. First, “s-p” splitting for electrons is bigger than for holes. For electrons, the magnitude of the splitting is about 45 meV and depends weakly on height. On the other hand, for holes, this splitting changes from  $\approx 20 \text{ meV}$  to nearly 5 meV when height changes from 20  $\text{ \AA}$  to 75  $\text{ \AA}$ . Second, the “p-p” splitting shows the opposite behavior. Namely, for holes the magnitude of the splitting remains nearly constant at approximately 4 meV, and for electrons it changes non-monotonically. It should be noted that the electronic “p-p” splitting is sensitive to alloy fluctuations and it can change by almost a factor of two by changing the alloy realization in the dot.<sup>45</sup>

For comparison, “s-p” and “p-p” splittings in a lens-shaped, non-alloyed  $\text{InAs}/\text{GaAs}$  dots with  $b = 252 \text{ \AA}$  also appear in Fig. 5. The pure dot has a “s-p” splitting for holes that is nearly the same as in the  $h = 35 \text{ \AA}$   $\text{In}_{0.6}\text{Ga}_{0.4}\text{As}/\text{GaAs}$  dot, while this splitting for electrons is nearly 20% bigger and depends weakly on height. In contrast, the “p-p” splitting for holes in the pure (non-alloyed  $\text{InAs}/\text{GaAs}$ ) dot is about twice as big as in the  $h = 35 \text{ \AA}$  alloy dot, and for electrons the “p-p” splitting depends weakly on height and is similar in magnitude to the splittings in alloy dots. It should be noted that in pure (non-alloyed  $\text{InAs}/\text{GaAs}$ ) dots the *hole* energy levels undergo a localization crossover (see discussion in Sec. III C) for tall dots, which render meaningless the notion of “s-p” and “p-p” splittings. (Such a localization crossover is absent for electrons.) For this reason, we have compared the splittings for the holes in a shallow ( $h = 35 \text{ \AA}$ ) non-alloyed  $\text{InAs}/\text{GaAs}$  dot only, while comparing the splitting for electrons in a range of heights.

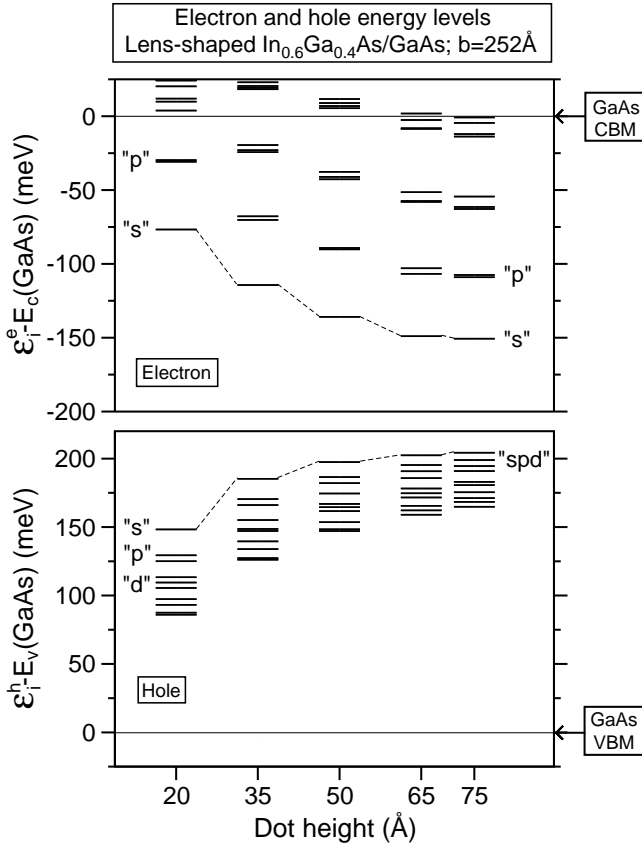


FIG. 4: First 20 electron (top panel) and hole (bottom) energy levels  $\mathcal{E}_n^e$  and  $\mathcal{E}_n^h$  for  $\text{In}_{0.6}\text{Ga}_{0.4}\text{As}/\text{GaAs}$  dots with different heights. The electron and hole energies are measured from GaAs CBM [ $E_c(\text{GaAs}) = -4.093 \text{ eV}$ ] and GaAs VBM [ $E_v(\text{GaAs}) = -5.620 \text{ eV}$ ], respectively. As height increases, the number of confined levels ( $\mathcal{E}_n^e < 0$  and  $\mathcal{E}_n^h > 0$ ) increases and the single-particle gap ( $\mathcal{E}_0^e - \mathcal{E}_0^h$ ) decreases. The confined electronic energy levels group in *non-degenerate shells* for all dots. “s”, “p”, and “d” indicate the predominant orbital character of selected states. For holes, up to  $h = 50 \text{ \AA}$  the second and third levels are “p”-like, while for larger heights these levels are “s”-“p” hybridized.

### B. Wavefunctions of confined states in $\text{In}_{0.6}\text{Ga}_{0.4}\text{As}/\text{GaAs}$ and non-alloyed $\text{InAs}/\text{GaAs}$ dots: mixed “s”+“p” character and “HH”+“LH” character

Figure 5 compares the wavefunctions of LUMO (lowest electron) and HOMO (highest hole) states as a function of height in  $\text{In}_{0.6}\text{Ga}_{0.4}\text{As}/\text{GaAs}$  dots with base  $b = 252 \text{ \AA}$ . To make the comparison, we plot isosurfaces that enclose 75% of the total charge density, and show contour plots taken at  $1 \text{ nm}$  above the dot’s base. In addition, the “s”-orbital character of the LUMO and HOMO is indicated as well as the HOMO’s heavy- and light-hole character. Further, for each height, the energy  $\mathcal{E}_0^e$  of LUMO is shown relative to  $E_c(\text{GaAs})$  and the energy of HOMO  $\mathcal{E}_0^h$  relative to  $E_v(\text{GaAs})$ . Prominent results are the following. *LUMO*: The lateral spatial extent of the

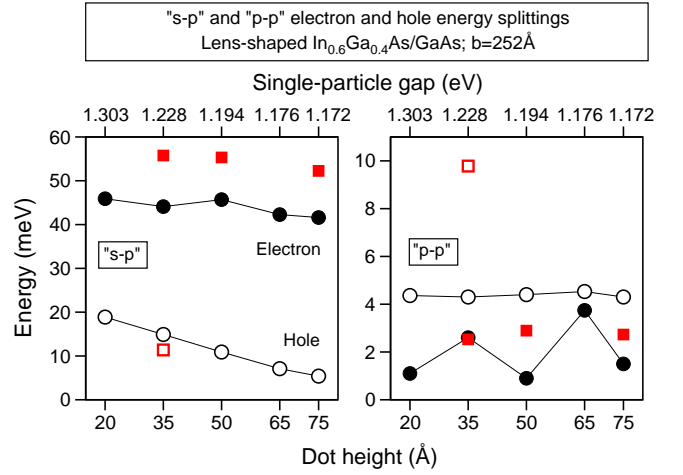


FIG. 5: Height dependence of the “s-p” ( $\mathcal{E}_1 - \mathcal{E}_0$ ) and “p-p” ( $\mathcal{E}_2 - \mathcal{E}_1$ ) energy splittings for electron and hole levels in  $\text{In}_{0.6}\text{Ga}_{0.4}\text{As}/\text{GaAs}$ . The single-particle gap is also shown. The “s-p” splitting for electrons is bigger than for holes; in turn, the “p-p” splitting shows the opposite trend. The height dependence of the “p-p” splitting for electrons is not monotonic, due to alloy fluctuations, while for holes this splitting remains nearly unchanged. For comparison, we show the “s-p” and “p-p” splittings for electron (solid squares) and hole (open squares) in non-alloyed  $\text{InAs}/\text{GaAs}$  dots.

wavefunction depends weakly on height. In contrast, as height decreases, the wavefunction extends into the barrier along the vertical direction. The “s”-orbital character of LUMO remains at nearly 90%. *HOMO*: Wavefunctions are more sensitive to height, showing a spatial extension that gets reduced significantly both in the lateral and vertical direction when height changes from  $75 \text{ \AA}$  to  $20 \text{ \AA}$ . This reduction leads to a strong localization at the center of the dot for  $h = 20 \text{ \AA}$ . The “s”-orbital character of the HOMO remains at about 90% up to  $h = 50 \text{ \AA}$ , for taller dots the character of the HOMO becomes “s” and “p” mixed. This mixing reflects the reduction of the hole charge density near the center of the dot. The heavy- (HH) and light-hole (LH) character also change with height in a similar manner as the “s” and “p” character. Namely, for the three smaller dots ( $20 \text{ \AA}$ ,  $35 \text{ \AA}$ ,  $50 \text{ \AA}$ ) the HOMO is mostly of the HH type, but as the height increases the LH character increases. We expect this behavior since the LH band-offset increases within the dot as height increases. (See Fig. 3.)

*Excited hole states*.—Figure 7 compares wavefunctions for excited hole states; namely, second (HOMO−1) and third (HOMO−2) hole states. As in Fig. 5, we show isosurfaces and contour plots, present the orbital and HH/LH character of these states, and the energies  $\mathcal{E}_1^h$  and  $\mathcal{E}_2^h$  for HOMO−1 and HOMO−2, respectively. The character of HOMO−1 and HOMO−2 are nearly the same at all heights. In addition, these states have a dominant “p”-orbital character for *all* heights, regardless the absence of “p”-shell structure for tall dots ( $h = 65 \text{ \AA}$  and  $75 \text{ \AA}$ ). (See Fig. 4) As in the case of the HOMO

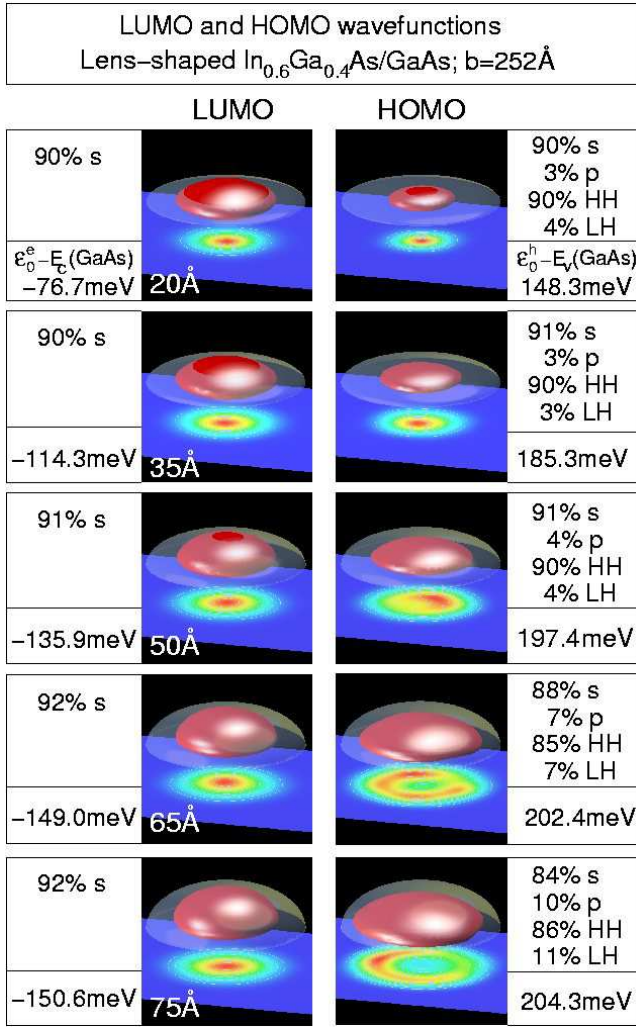


FIG. 6: Height dependence of lowest electron level (LUMO) and highest hole level (HOMO) wavefunctions. Isosurfaces enclose 75% of the total charge density. Countours are taken at a plane 1 nm above the base. The energy relative to  $E_c(\text{GaAs})$  and  $E_v(\text{GaAs})$  is shown. The “s-” and “p-” orbital character (see Eq. 7), and the heavy-hole (HH) and light-hole (HH) character are indicated. For the tallest dot, the wavefunctions are entirely confined within the dot and the effective size of the dot—spatial extent of the wavefunctions—is nearly the same for LUMO and HOMO. For shorter dots the effective size gets significantly reduced for the HOMO while it remains nearly unchanged for the LUMO.

state, the HOMO-1 and HOMO-2 states have increasing light-hole character with increasing height. However, the percentage of light-hole character is almost twice that of HOMO. For instance, at  $h = 75\text{\AA}$ , the LH character of the HOMO-2 is 17% while the HOMO LH character is 11%.

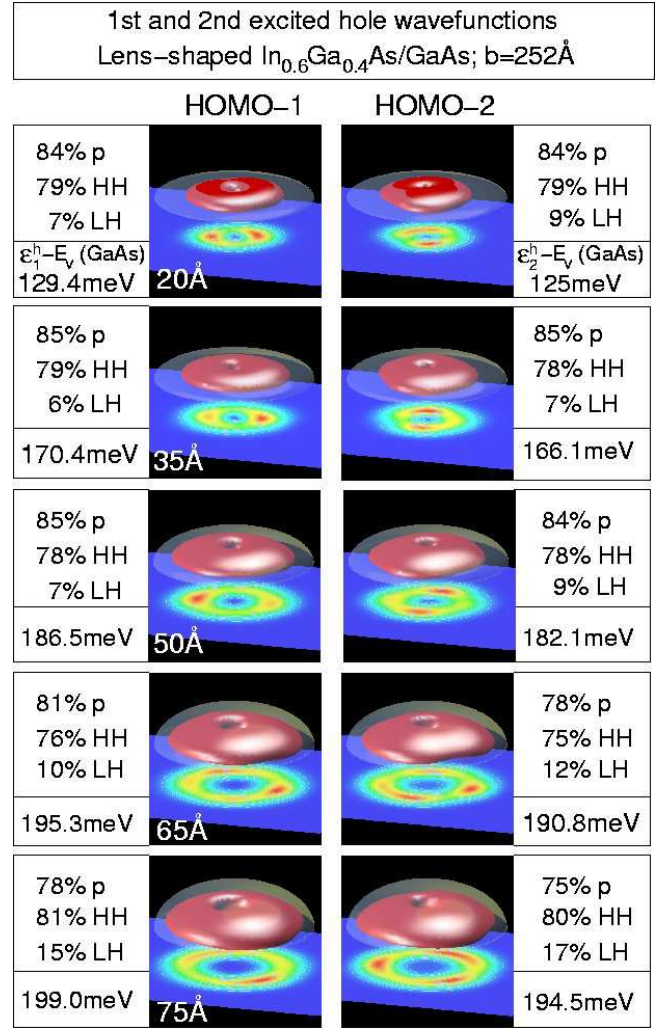


FIG. 7: Wavefunctions of the first 2 excited hole levels HOMO-1 and HOMO-2 for different dot’s height. As in Fig. 6, the isosurface encloses 75% of the total charge density and the countours are taken at 1nm above the base. Labels indicate the “p” orbital character, the heavy- and light-hole characters and the energy of the states relative to  $E_v(\text{GaAs})$ .

### C. Strain-driven hole localization

For dots containing both Ga and In ( $\text{In}_{0.6}\text{Ga}_{0.4}\text{As}/\text{GaAs}$ ) with  $b = 252\text{\AA}$  and heights in the range 20-75 $\text{\AA}$ , we have shown that the wavefunctions of HOMO ( $\mathcal{E}_0^h$ ) and HOMO-1 ( $\mathcal{E}_1^h$ ), as well as other low-lying excited hole states, are localized inside the dot (see Figs. 6 and 7) and that these levels have a sizeable “s-p” splitting  $\mathcal{E}_1^h - \mathcal{E}_0^h$  (see Fig. 5). In contrast, in lens-shaped pure, non-alloyed InAs/GaAs quantum dots, localization of the low-lying hole states at the dot interface develops as the height of the dot increases. In addition, HOMO and HOMO-1 become nearly degenerate [e. g.,  $\mathcal{E}_0^h - E_v(\text{GaAs}) = 256.2\text{meV}$  and  $\mathcal{E}_1^h - E_v(\text{GaAs}) = 255.7\text{meV}$  at  $h = 75\text{\AA}$ ], as well as HOMO-2 and HOMO-3. (It should also be



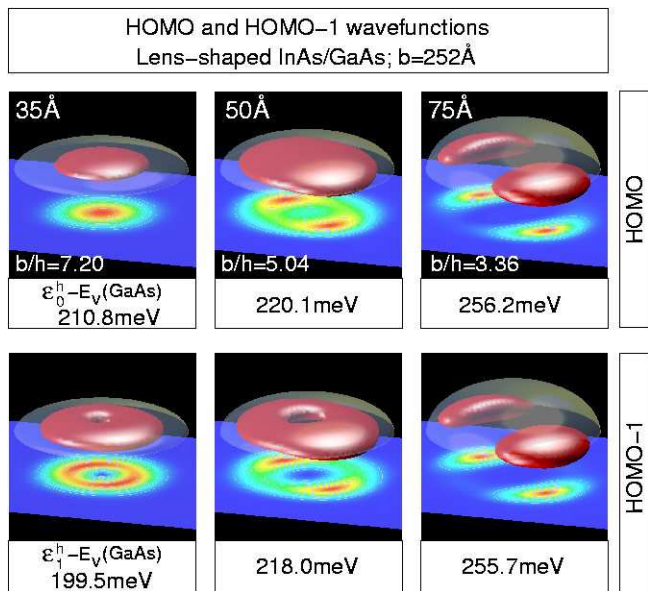


FIG. 8: HOMO and HOMO-1 wavefunctions in pure, non-alloyed InAs/GaAs lens-shaped quantum dot as a function of height. The dots have the same base diameter  $b = 252\text{\AA}$ . The aspect ratio  $b/h$  is shown, as well as the energy relative to  $E_v(\text{GaAs})$ . As before, the isosurfaces enclose 75% of the charge density and the contours are taken at 1 nm above the base. As height increases, interface localization takes place, and the HOMO and HOMO-1 become nearly degenerate.

noted that for the flat dot the energies of HOMO and HOMO-1 are bigger than in the alloy dot of the same size.) Remarkably, HOMO and HOMO-1 are *polarized* along  $[1\bar{1}0]$  (Fig. 8) while HOMO-2 and HOMO-3 (not shown) are polarized along  $[110]$ . Figure 8 shows the development of this interfacial localization and the energy of HOMO and HOMO-1 relative to  $E_v(\text{GaAs})$ . As in Figs. 6 and 7, isosurfaces enclose 75% of the HOMO and HOMO-1 total charge density.

It should be noted that the pure, non-alloyed InAs/GaAs dots have the *same* base size and *same* height range as the alloy dots we have previously discussed. Hence, hole localization does not have its origin on geometrical aspects of the quantum dots. Instead, the localization of the hole wavefunctions is driven by the biaxial strain present in the nanostructure (QD+GaAs matrix). To explain this result, we plot in Fig. 9(a) the valence band offsets of heavy-hole (HH) and light-hole (LH) character (inside the dot) along the line  $\overleftrightarrow{OO'}$  (see Figs. 1 and 3) and the energy of HOMO and HOMO-1 (thick dashes). In addition, we plot in Fig. 9(b) a 3-dimensional rendering of the higher energy hole band offset values at a plane normal to  $\overleftrightarrow{OO'}$ , cut slightly above the base of the dot. *First*, we see that as the dot height increases the pocket structure [indicated with arrows in Fig. 9(a)] that appears in the higher energy band offset dramatically widens the confining potential (given by the band

offset) along  $\overleftrightarrow{OO'}$  and that the band offsets values decrease. Further, the band offset become asymmetric with the values at the top of the dot *smaller* than at the *base*. As a consequence, it becomes clear why the energy of the HOMO and HOMO-1 become bigger and we also expect the wavefunctions of these states to be localized near the base of the dot. It is important to mention that in the calculation of the energy of the HOMO and HOMO-1 we do not utilize the band offset we present in Fig. 9(a). *Second*, the band offsets shown in Fig. 9 present a “crown” structure at the dot-matrix interface.<sup>46</sup> This crown structure becomes more significant as height increases, as a consequence of the values of band offset along the  $[110]$  and  $[1\bar{1}0]$  direction presenting a weak dependence on height. *Finally*, the localization of the low-lying hole wave functions that develops as the height of pure, non-alloyed InAs/GaAs lens-shaped quantum dots is a result of the peculiar characteristics of the higher energy valence-band offsets, which in turn are determined by the biaxial strain profile in the nanostructure.

Finally, it should be noticed that electron states do not experience interface localization; instead, they continue to form shells and the levels in these shells have a predominant, not-mixed orbital character (“s”, “p”, ...). The reason for the absence of electron localization is that electron states are sensitive to the (hydrostatic) isotropic strain rather than to the biaxial strain.

#### D. Exciton transitions

Figure 10 shows the lowest bright transition (gap) of the exciton as a function of dot height, calculated at the single-particle (SP) level ( $\mathcal{E}_0^e - \mathcal{E}_0^h$ ) and by using the many-body, configuration interaction (CI) method.<sup>42</sup> In the latter, we use a basis consisting of 12 electron and 20 hole confined levels ( $n_e = 12, n_h = 20$ ) for heights  $h = 35-75\text{\AA}$  and ( $n_e = 6, n_h = 20$ ) for  $h = 20\text{\AA}$ . As expected, the transition energy decreases as height increases, due to confinement. However, the scaling with height differs significantly from predictions of single-band, effective mass ( $\sim h^{-2}$ ).<sup>47</sup> Namely, by fitting our results for the height dependence of the gap to the function  $a + b/h^\gamma$  we find  $\gamma^{SP} = 0.95$  and  $\gamma^{CI} = 1.09$ . The value of the gap for large heights correspond, respectively, to  $a^{SP} = 1.117\text{ eV}$  and  $a^{CI} = 1.116\text{ eV}$  in the single-particle and CI approach. We expect the SP and CI scaling exponents to be different, as in the single-particle calculation the scaling is dictated by the scaling of the LUMO and HOMO, whereas in the CI calculation the electron-hole matrix elements are also included and the magnitude of these matrix elements decreases with height. The discrepancy between the scaling ( $\gamma$ ) in single-band effective mass and both our SP and CI calculations can be attributed to non-trivial effects that are naturally accounted for within our atomistic approach such as non-parabolicity and multi-band effects, and the position-dependent strain present in the nanostructure. The values of  $a$  at large heights is also

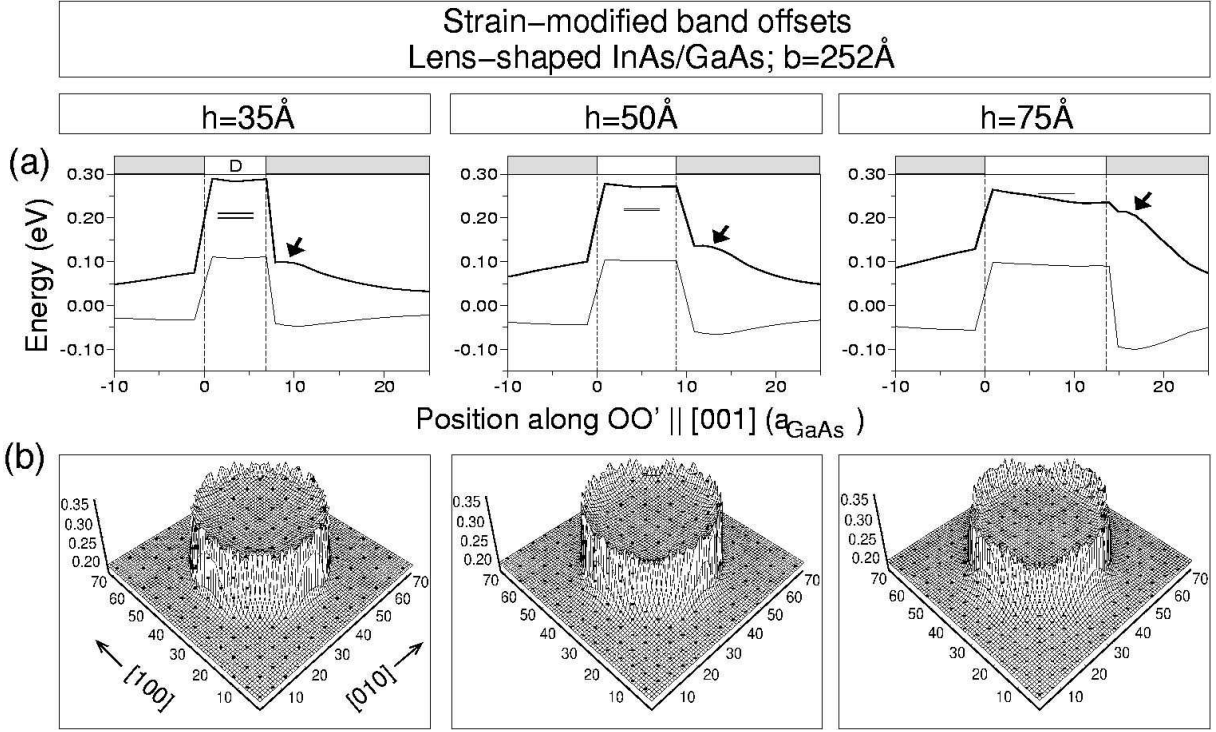


FIG. 9: Strain-modified band offsets in a pure, lens-shaped, non-alloyed InAs/GaAs quantum dot along the  $OO'$  direction (a) and in a plane normal to latter cut at a height slightly above the base of the dot (b). Dashes in panel (a) correspond to the HOMO and HOMO-1 energy levels. The splitting among these levels decreases with the dot height. Arrows indicate pocket formation (see also Fig. 3) in the band offset due to strain accumulation at the dot-matrix interface at the top of the dot.

expected to be different, and the difference is attribute to correlation effects that are present in the many-body configuration approach. Thus, we expect a small difference ( $\sim$  meV) between  $a^{SP}$  and  $a^{CI}$ .

For comparison, we also present results for the lowest exciton transition [squares, open (SP) and solid (CI)] in lens-shaped, non-alloyed InAs/GaAs quantum dot. Th values of the transition energies are smaller than in th alloy dots.

#### IV. SUMMARY

By using a high-level atomistic approach, we hav predicted spectroscopic characteristics of self-assemble  $\text{In}_{1-x}\text{Ga}_x\text{As}/\text{GaAs}$  quantum dots as a function of heigh and composition. Several prominent features emerged.

(i) The biaxial strain at the dot-GaAs matrix inter face increases with height, whereas, regardless of height the strain is negligibly small along the  $[011]$ ,  $[0\bar{1}\bar{1}]$  an crystallographically equivalent directions.

(ii) Regardless of height and composition, the confined electron energy levels group in shells of nearly degenerate states. The average energy splitting among these shells depends weakly on height; however, this splitting is larger in pure, non-alloyed InAs/GaAs. In contrast, the confined hole energy levels form shells only in flat dots

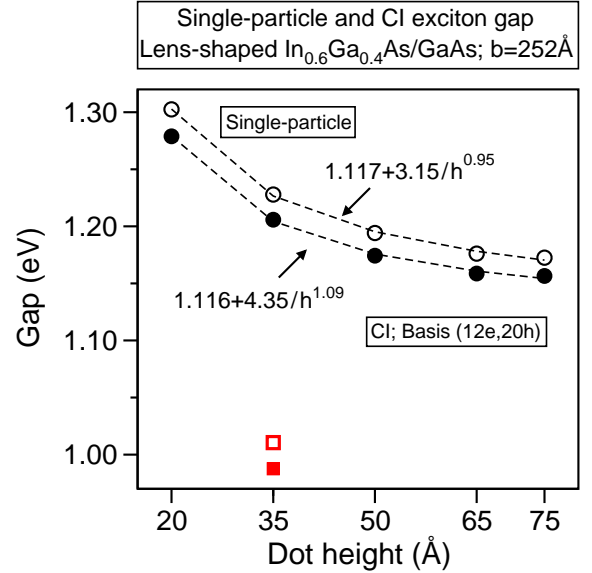


FIG. 10: Exciton gap as a function of height. Single-particle (open circles) and configuration interaction (CI, solid circled) results are shown. The CI basis is  $(n_e = 12, n_h = 20)$  for  $h = 35-75 \text{ \AA}$  and  $(n_e = 6, n_h = 20)$  for  $h = 20 \text{ \AA}$ . Dashed lines represent fits to the function  $a + b/h^\gamma$ . Fitting parameters are indicated. For comparison, we present results [squares; open (SP) and solid (CI)] for a pure, non-alloyed InAs/GaAs dot.

and near the highest hole level (HOMO).

(iii) In alloy dots, the *electrons*' "s-p" splitting depends weakly on height, while the "p-p" splitting depends non-monotonically—due to alloy fluctuations. In pure, non-alloyed InAs/GaAs dots, *both* these splittings depend weakly on height. Further, the "s-p" splitting is larger while the "p-p" has nearly the same magnitude. For *holes* levels in alloy dots, the "s-p" splitting decreases with increasing height (the splitting in tall dots being about 4 times smaller than in flat dots), whereas the "p-p" splitting remains nearly unchanged. Shallow pure dots have a "s-p" splitting of nearly the same magnitude, whereas the "p-p" splitting is about three times larger.

(iv) As height increases, the "s" and "p" character of the wavefunction of the HOMO becomes mixed, and so does the heavy- and light-hole character.

(v) In alloy dots, regardless of height, the wavefunction of low-lying (near the HOMO) hole states are localized inside the dot. Remarkably, in pure, non-alloyed InAs/GaAs dots, as the dot height increases, these states become localized at the dot-matrix interface and nearly degenerate. Further, the localized states are polarized along  $[1\bar{1}0]$  (HOMO and HOMO-1) and  $[110]$  (HOMO-2 and HOMO-3). This localization effect is driven by the peculiarities of the biaxial strain present in the nanostructure.

(vi) The lowest exciton transition energy (gap) decreases with height, but the scaling (roughly  $\sim h^{-1}$ ) differs significantly from the prediction of single-band effective mass ( $\sim h^{-2}$ ).

The study we presented here may be used to bridge spectroscopy results with theory without the need for severe theoretical approximations.

### Acknowledgments

This work has been supported by DOE-SC-BES-DMS under grant No. DE-AC36-99GO10337.

## APPENDIX A: CONVERGENCE

The LCBB method contains several convergence parameters: supercell size, number of bulk materials ( $M$ ), number of bands ( $n$ ), and number of  $\mathbf{k}$  points. The choice of bulk materials and number of bands can be physically motivated and justified, whereas the choice of supercell size and number of  $\mathbf{k}$  points is not as clear. For this reason, we conducted a convergence assessment on supercell size and number of  $\mathbf{k}$  points. As for the bulk materials, we choose (i) *unstrained* GaAs and (ii) InAs subject to strain values of  $\varepsilon_{xx} = \varepsilon_{yy} = -0.06$ , and  $\varepsilon_{zz} = +0.04$ .

These values are typical of strain inside a non-alloyed InAs/GaAs lens-shaped quantum dot. For the bands  $n$ , when simulating the *electron* and *hole* energy levels we use respectively the lowest *conduction* band and the three highest valence bands of both bulk materials.

*Supercell size.*—We consider cubic supercells of size  $L_x \times L_y \times L_z$ , where  $L_t$  ( $t = x, y, z$ ) is measured in units of the lattice parameter of bulk GaAs  $a_{GaAs}$ . Based on strain calculations (see above), we selected a supercell size such that the strain profile within the quantum dot remained unchanged upon changing size. Notwithstanding, it should be noted that although the strain may be converged within the dot the strain values at the boundary of the supercell may not be zero due to the slow relaxation of the strain fields. This residual strain introduces small changes ( $\sim$  meV) in the energy levels. For instance, Figure 1 shows the effect of reducing the residual strain by changing the supercell size from  $72 \times 72 \times 40$  to  $72 \times 72 \times 48$  for a  $h = 20 \text{ \AA}$  dot.

*Number of  $\mathbf{k}$  points.*—The  $\mathbf{k}$ -point meshes enclose all the  $\mathbf{k}$  vectors around the  $\Gamma$  point that lie within an ellipsoid with main axis equal to  $(2\pi/L_x)P$ ,  $(2\pi/L_y)Q$ , and  $(2\pi/L_z)K$ , respectively.  $P$ ,  $Q$ , and  $K$  give the number of  $\mathbf{k}$  points taken along each cartesian direction. In our convergence assesment  $P = 6, 8$ ,  $Q = P$ , and  $K$  ranges from 8-18. Figure 11 shows the electron energy levels for several dots as a function of  $\mathbf{k}$ -point mesh. We distinguish several features. (a) When compared with the energy of the levels, differences in energies are quicker to converge. (b) High-energy levels require larger  $\mathbf{k}$ -point meshes to converge within a given threshold. (c) The taller the quantum dots the smaller the number of  $\mathbf{k}$  points needed to converge. (d) The use of  $(6, 6, K)$  and  $(8, 8, K)$   $\mathbf{k}$ -point meshes results in similar energies for the lowest electron level. The discrepancy between the predictions made with these two meshes increases for high-energy levels.

To present details of the convergence with respect to  $\mathbf{k}$ -point mesh, Figure 12 shows a convergence assessment of HOMO and LUMO's energy in flat ( $h = 20 \text{ \AA}$ ) and tall ( $h = 75 \text{ \AA}$ ) dots. The energy of HOMO converges visibly quicker than that of LUMO. This behavior holds for all hole energy levels, and arises from the higher size (three  $\Gamma_{15v}$  bands) of the basis used in the simulation.

To summarize, the results we present in this work for each quantum dot derive from simulations with  $\mathbf{k}$ -point meshes that provide with energy levels converged within 2meV. Table I shows the supercell sizes and  $\mathbf{k}$ -point meshes we have used to simulate the electronic structure of each of the dots we have studied. It should be noted that *energy differences* are converged to much less than this lower bound.

<sup>1</sup> S. Fafard, R. Leon, D. Leonard, J. L. Merz and P. M. Petroff, Phys. Rev. B **52**, 5752 (1995); S. Fafard, D.

Leonard, J. L. Merz, and P. M. Petroff, Appl. Phys. Lett.

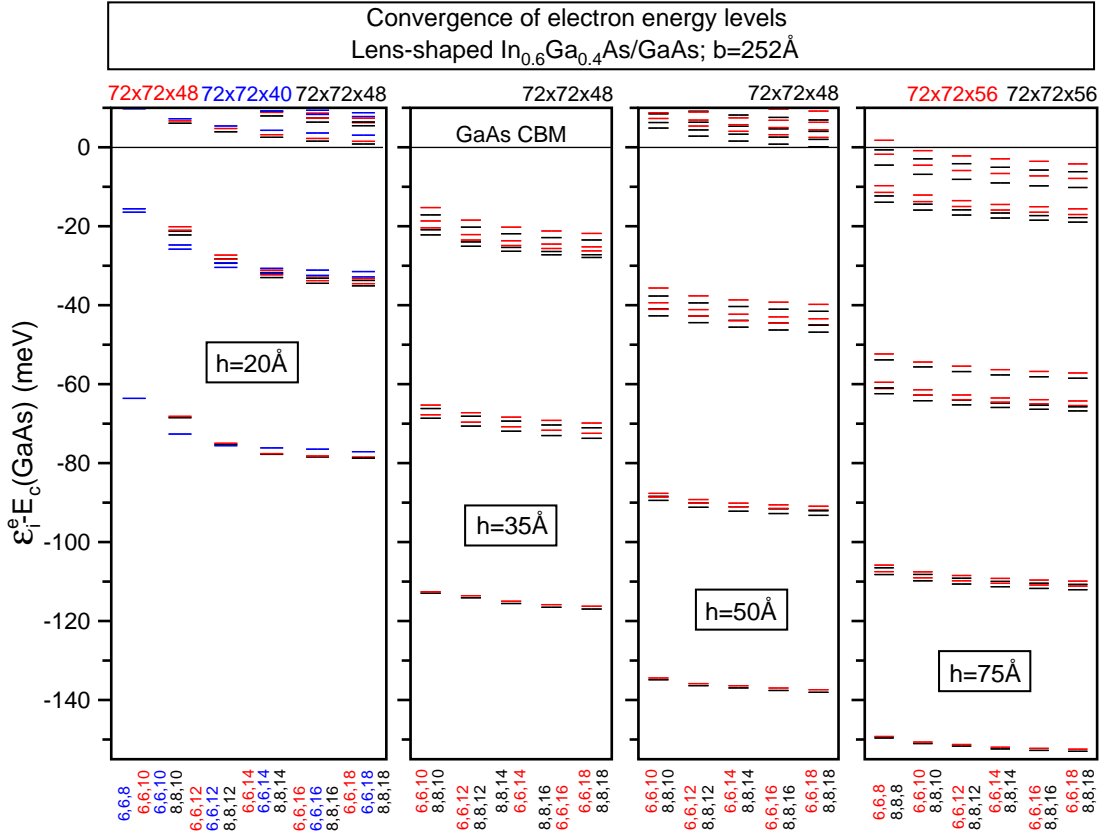


FIG. 11: Convergence of the first 20 (including Kramers degeneracy) electron energy levels  $\mathcal{E}_n^e$  of dots with different heights as a function of  $\mathbf{k}$ -point meshes and for different supercell sizes  $[(L_x \times L_y \times L_z)]$ . The results are color coded to help clarity, and are given w.r.t. GaAs CBM [ $E_c(\text{GaAs}) = -4.093 \text{ eV}$ ]. The basis encompass single-band,  $\Gamma_{1c}$  GaAs and strained-InAs bulk Bloch functions in the vicinity of the  $\Gamma$  point of the supercell. The 3-fold  $(Q, Q, K)$  represents the main-axis sizes of an ellipsoid in reciprocal space. This ellipsoid determines the number of  $\mathbf{k}$  points in the basis, which is the *same* for GaAs and InAs.

TABLE I: Summary of supercell sizes  $L_x \times L_y \times L_z$  (lengths in units of  $a_{\text{GaAs}}$ ) and  $\mathbf{k}$ -point meshes  $(Q, Q, K)$  used in the simulations. Dot's base  $b = 252 \text{ \AA}$ . (c.f. Fig. 1 for dot's geometry.)

height (Å)	$L_x \times L_y \times L_z$	$\mathbf{k}$ -point mesh
20	$72 \times 72 \times 48$	(6, 6, 13)
35	$72 \times 72 \times 48$	(6, 6, 13)
50	$72 \times 72 \times 48$	(6, 6, 12)
65	$72 \times 72 \times 48$	(6, 6, 12)
75	$72 \times 72 \times 56$	(6, 6, 10)

- 65, 1388 (1994); J.-Y. Marzin, J.-M. Gérard, A. Izraël, D. Barrier, G. Bastard, Phys. Rev. Lett. **73**, 716 (1994); M. Grundmann, J. Christen, N. N. Ledentsov, J. Böhrer, D. Bimberg, S. S. Ruvimov, P. Werner, U. Richter, U. Gösele, J. Heydenreich, V. M. Ustinov, A. Yu. Egorov, A. E. Zhukov, P. S. Kop'ev, and Zh. Alferov, Phys. Rev. Lett. **74**, 4043 (1994).
- <sup>2</sup> F. Guffarth, R. Heitz, A. Schliwa, O. Stier, M. Geller, C. M. A. Kapteyn, R. Sellin, and D. Bimberg, Phys. Rev. B **67**, 235304 (2003); J. J. Finley, A. D. Ashmore, A. Lemaitre, D. J. Mowbray, M. S. Skolnick, I. E. Itskevich, P. A. Maksym, M. Hopkinson, and T. F. Krauss, Phys.

- Rev. B **63**, 073307 (2001); R. J. Warburton, C. S. Dürr, K. Karrai, J. P. Kotthaus, G. Medeiros-Ribeiro, and P. M. Petroff, Phys. Rev. Lett. **79**, 5282 (1997).
- <sup>3</sup> J. J. Finley, P. W. Fry, A. D. Ashmore, A. Lemaitre, A. I. Tartakovskii, R. Oulton, D. J. Mowbray, M. S. Skolnick, M. Hopkinson, P. D. Buckle, P. A. Maksym, Phys. Rev. B **63**, 161305 (2001).
- <sup>4</sup> M. Bayer, O. Stern, P. Hawrylak, S. Fafard, and A. Forchel, Nature **405**, 923 (2000); E. Dekel, D. Gershoni, E. Ehrenfreund, J. M. Garcia, and P. Petroff, Phys. Rev. B **61**, 11009 (2000); F. Findeis, A. Zrenner, G. Böhm, and G. Abstreiter, Solid State Comm. **114**, 227 (2000); L. Landin, M. S. Miller, M.-E. Pistol, C. E. Pryor, and L. Samuelson, Science **280**, 262 (1998); M. Bayer, T. Gutbrod, A. Forchel, V. D. Kulakovskii, A. Gorbunov, M. Michel, R. Steffen, and K. H. Wang, Phys. Rev. B **58**, 4740 (1998).
- <sup>5</sup> E. Dekel, D. Gershoni, E. Ehrenfreund, D. Spektor, J. M. Garcia, and P. M. Petroff, Phys. Rev. Lett. **80**, 4991 (1998).
- <sup>6</sup> B. Urbaszek, R. J. Warburton, K. Karrai, B. D. Gerardot, P. M. Petroff, and J. M. Garcia, Phys. Rev. Lett. **90**, 247403 (2003); M. Bayer, G. Ortner, O. Stern, A. Kuther, A. A. Gorbunov, A. Forchel, P. Hawrylak, S. Fafard, K. Hinzer, T. L. Reinecke, S. N. Walck, J. P. Reithmaier, F. Klopff, and F. Schäfer, Phys. Rev. B **65**, 195315 (2002); J.

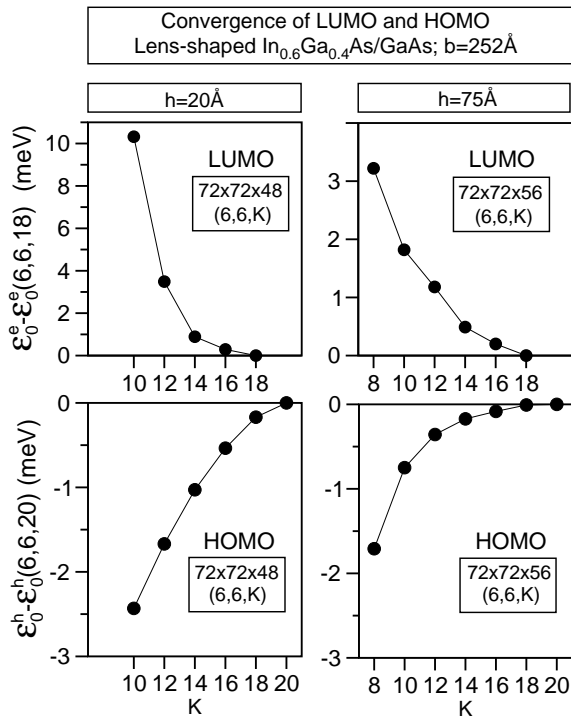


FIG. 12: Convergence of LUMO ( $\mathcal{E}_0^e$ ) and HOMO ( $\mathcal{E}_0^h$ ) energies relative to their value simulated with the highest number of  $\mathbf{k}$  points on a basis of the form (6, 6,  $K$ ). To simulate the HOMO energy we include the 3  $\Gamma_{15v}$  bands. The size of the supercell is indicated.

J. Finley, D. J. Mowbray, M. S. Skolnick, A. S. Ashmore, C. Baker, A. F. G. Monte, and M. Hopkinson, Phys. Rev. B **66**, 153316 (2002).

<sup>7</sup> A. Zunger, phys. stat. sol. (a) **190**, 467 (2002).

<sup>8</sup> L. He, G. Bester, and A. Zunger, Phys. Rev. B **70**, 235316 (2004).

<sup>9</sup> G. Bester, S. Nair, A. Zunger, Phys. Rev. B **67**, 161306 (2003).

<sup>10</sup> G. Bester and A. Zunger, Phys. Rev. B **68**, 073309 (2003).

<sup>11</sup> J. Simonin, C. R. Proetto, Z. Barticevic, and G. Fuster, Phys. Rev. B **70**, 205305 (2004).

<sup>12</sup> A. Wojs, P. Hawrylak, S. Fafard, and L. Jacak, Phys. Rev. B **54**, 5604 (1996).

<sup>13</sup> J. Shumway, A. J. Williamson, A. Zunger, A. Passaseo, M. DeGiorgi, R. Cingolani, M. Catalano, and P. Crozier, Phys. Rev. B **64**, 125302 (2001).

<sup>14</sup> A. J. Williamson, L. W. Wang, and A. Zunger, Phys. Rev. B **62**, 12963 (2000).

<sup>15</sup> N. Liu, H. K. Lyeo, and C. K. Smith, Appl. Phys. Lett. **80**, 4345 (2002).

<sup>16</sup> D. M. Bruls, J. W. A. M. Vugs, P. M. Koenraad, H. W. M. Salemik, J. H. Wolter, M. Hopkinson, M. S. Skolnick, F. Long, and S. P. A. Gill, Appl. Phys. Lett. **81**, 1708 (2002).

<sup>17</sup> Q. Gong, P. Offeremans, R. Nötzel, P. M. Koenraad, and J. H. Wolter, Appl. Phys. Lett. **85**, 5697 (2004).

<sup>18</sup> L. Jacak, P. Hawrylak, A. Wojs, *Quantum Dots* (Springer, Berlin, 1997).

<sup>19</sup> M. A. Cusak, P. R. Briddon, and M. Jaros, Phys. Rev. B **54**, R2300 (1996); J. Marzin and G. Bastard, Solid State. Comm. **92**, 437 (1994).

<sup>20</sup> C. Pryor, Phys. Rev. B **57**, 7190 (1998); T. B. Bahder, Phys. Rev. B **45**, 1629 (1992); T. B. Bahder, Phys. Rev. B **41**, 11992 (1990) [see also T. B. Bahder, Phys. Rev. B **46**, 9913 (1992)] and references therein.

<sup>21</sup> L.-W. Wang and A. Zunger, Phys. Rev. B **59**, 15806 (1999).

<sup>22</sup> L. W. Wang, A. J. Williamson, A. Zunger, H. Jiang, and J. Singh, Appl. Phys. Lett. **76**, 339 (2000).

<sup>23</sup> A. Zunger, phys. stat. sol. (b) **224**, 727 (2001).

<sup>24</sup> S. Lee, O. L. Lazarenkova, P. von Allmen, F. Oyafuso, and G. Klimeck, Phys. Rev. B **70**, 125307 (2004); R. Santoprete, B. Koiler, R. B. Capaz, P. Kratzer, Q. K. K. Liu, and M. Scheffler, Phys. Rev. B **68**, 235311 (2003); G. W. Bryant and W. Jaskólski, Phys. Rev. B **67**, 205320 (2003); S. Lee, L. Jönsson, J. W. Wilkins, G. W. Bryant, G. Klimeck, Phys. Rev. B **63**, 195318 (2001); Kevin Leung and K. B. Whaley, Phys. Rev. B **56**, 7455 (1997).

<sup>25</sup> R. Ferreira, Physica E **13**, 216 (2002).

<sup>26</sup> M. Grundmann, O. Stier, and D. Bimberg, Phys. Rev. B **52**, 11969 (1995).

<sup>27</sup> O. Stier, M. Grundmann, and D. Bimberg, Phys. Rev. B **59**, 5688 (1999).

<sup>28</sup> F. Guffarth, R. Heitz, A. Schliwa, O. Stier, N. N. Ledentsov, A. R. Kovsh, V. M. Ustinov, and D. Bimberg, Phys. Rev. B **64**, 085305 (2001).

<sup>29</sup> R. Heitz, S. Rodt, A. Schliwa, and D. Bimberg, phys. stat. sol. (b) **238**, 273 (2003); O. Stier, R. Heitz, A. Schliwa, and D. Bimberg, phys. stat. sol. (a) **190**, 477 (2002).

<sup>30</sup> J. Kim, L. W. Wang, and A. Zunger, Phys. Rev. B. **57**, R9408 (1998).

<sup>31</sup> C. Pryor, Phys. Rev. B **60**, 2869 (1999).

<sup>32</sup> D. Leonard, M. Krishnamurthy, C. M. Reaves, S. P. Denbaars, and P. M. Petroff, Appl. Phys. Lett. **63**, 3203 (1993); D. Leonard, K. Pond, and P. M. Petroff, Phys. Rev. B **50**, 11687 (1994); S. Raymond, S. Fafard, P. J. Poole, A. Wojs, P. Hawrylak, and S. Charbonneau, D. Leonard, R. Leon, P. M. Petroff, and J. L. Merz, Phys. Rev. B **54**, 11548 (1996); Z. R. Wasilewski, S. Fafard, and J. P. McCaffrey, J. Cryst. Growth **201-202**, 1131 (1999); A. G. Cullis, D. J. Norris, T. Walthers, M. A. Migliorato, and M. Hopkinson, Phys. Rev. B **66**, 081305 (2002); S. Anders, C. S. Kim, B. Klein, M. W. Weller, and R. P. Mirin, Phys. Rev. B **66**, 125309 (2002).

<sup>33</sup> M. Tadić, F. M. Peeters, K. L. Janssens, M. Korkusinski, and P. Hawrylak, J. Appl. Phys. **92**, 5819 (2002).

<sup>34</sup> C. Pryor, J. Kim, L. W. Wang, A. J. Williamson, and A. Zunger, J. Appl. Phys. **83**, 2548 (1998).

<sup>35</sup> R. M. Martin, Phys. Rev. B **1**, 4005 (1970); P. N. Keating, Phys. Rev. **145**, 637 (1966).

<sup>36</sup> G. Bester and A. Zunger, Phys. Rev. B **71**, 045318 (2005).

<sup>37</sup> W. Sheng and J.-P. Leburton, phys. stat. sol. (b) **237**, 394 (2003); O. Stier, *Electronic an Optical Properties of Quantum Dots and Wires* (Wissenschaft & Technik Verlag, Berlin, 2001).

<sup>38</sup> C. Pryor, M.-E. Pistol, and L. Samuelson, Phys. Rev. B **56**, 10404 (1997).

<sup>39</sup> O. L. Lazarenkova, P. von Almen, F. Oyafuso, S. Lee, and G. Klimeck, Appl. Phys. Lett. **85**, 4193 (2004).

<sup>40</sup> J. D. Eshelby, J. Appl. Phys. **25**, 255 (1954).

<sup>41</sup> S.-H. Wei and A. Zunger, Phys. Rev. B **49**, 14337 (1994).

<sup>42</sup> A. Franceschetti, H. Fu, L. W. Wang, and A. Zunger, Phys. Rev. B **60**, 1819 (1999).

<sup>43</sup> R. Resta, Phys. Rev. B **16**, 2717 (1977).

<sup>44</sup> This shell-structure feature qualitatively agrees with the

prediction of a single-band, effective mass two-dimensional harmonic oscillator (see Ref. 18).

<sup>45</sup> G. A. Narvaez, G. Bester, and A. Zunger (unpublished).

<sup>46</sup> These “crown” structure has been predicted by He and coworkers in Ref.<sup>8</sup> and has been argued that it is this structure that is responsible for similar localization of hole wavefunctions found in large, non-alloyed InAs/GaAs *spherical* quantum dots.<sup>8</sup>

<sup>47</sup> For single-band effective mass calculations of the single-particle electronic levels in lens-shaped semiconductor quantum dots with aspect ratio  $h/b = 0.25$  and  $0.5$  see J. Even and S. Loualiche, J. Phys. A: Math. Gen. **36**, 11677 (2003) and A. H. Rodriguez, C. Trallero-Giner, S. E. Ulloa, and J. Marín-Antuña, Phys. Rev. B **63**, 125319 (2001), respectively.